Document Version
Publisher's PDF, also known as Version of record

Link to publication record in King's Research Portal

Magphan® Phantoms for MR for radiation therapy and quantitative imaging applications.

Magphan® S162 & 128

SN:1620012

SN:1280001

Smári

Sub-voxel geometric distortion measurements and critical image quality metrics engineered for ease of use in the clinical workflow.

The Phantom Laboratory manufactures high-precision phantoms coupled with Smári image analysis service and innovative custom solutions for the medical imaging and radiation therapy fields.

Click to see our latest phantoms and schedule a demo of our Smári image analysis service.

phantomlab

phantomlab.com

REVIEW ARTICLE

Input function and modeling for determining bone metabolic flux using [^{18}F] sodium fluoride PET imaging: A step-by-step guide

Tanuj Puri[1,2] | Michelle L. Frost[3] | Amelia E. B. Moore[2] | Gary J. R. Cook[4] | Glen M. Blake[2]

[1]Faculty of Biology, Medicine and Health, School of Medical Sciences, Division of Cancer Sciences, The University of Manchester, The Christie NHS Foundation Trust, Manchester, UK

[2]Department of Biomedical Engineering, School of Biomedical Engineering and Imaging Sciences, King's College London, St. Thomas' Hospital, London, UK

[3]Institute of Cancer Research Clinical Trials & Statistics Unit (ICR-CTSU), The Institute of Cancer Research, Sutton, UK

[4]Department of Cancer Imaging, School of Biomedical Engineering and Imaging Sciences, King's College London, St. Thomas' Hospital, London, UK

Correspondence
Tanuj Puri, PhD, Postdoctoral Research Associate at The University of Manchester, Faculty of Biology, Medicine and Health, School of Medical Sciences, Division of Cancer Sciences, The Christie NHS Foundation Trust, Radiotherapy Related Research, Wilmslow Road, Manchester M20 4BX, UK
Email: tanuj.puri@manchester.ac.uk, tanujpuri82@gmail.com

Abstract

Studies of skeletal metabolism using measurements of bone metabolic flux (K_i) obtained with [^{18}F] sodium fluoride ([^{18}F]NaF) positron emission tomography (PET) scans have been used in clinical research for the last 30 years. The technique has proven useful as an imaging biomarker in trials of novel drug treatments for osteoporosis and investigating other metabolic bone diseases, including chronic kidney disease mineral and bone disorder. It has also been shown to be valuable in metastatic bone disease in breast cancer patients and may have potential in other cancer types, such as prostate cancer, to assess early bone fracture risk. However, these studies have usually required a 60-min dynamic PET scan and measurement of the arterial input function (AIF), making them difficult to translate into the clinic for diagnostic purposes. We have previously proposed a simplified method that estimates the K_i value at an imaging site from a short (4-min) static scan and venous blood samples. A key advantage of this method is that, by acquiring a series of static scans, values of K_i can be quickly measured at multiple sites using a single injection of the tracer. To date, the widespread use of [^{18}F]NaF PET has been limited by the need to measure the AIF required for the mathematical modeling of tracer kinetics to derive K_i and other kinetic parameters. In this report, we review different methods of measuring the AIF, including direct arterial sampling, the use of a semi-population input function (SP-AIF), and image-derived input function, the latter two requiring only two or three venous blood samples obtained between 30 and 60 min after injection. We provide an SP-AIF model and a spreadsheet for calculating K_i values using the static scan method that others can use to study bone metabolism in metabolic and metastatic bone diseases without requiring invasive arterial blood sampling. The method shortens scan times, simplifies procedures, and reduces the cost of multicenter trials without losing accuracy or precision.

KEYWORDS
[^{18}F] sodium fluoride, arterial input function, bone metabolism, modeling, PET imaging

1 | INTRODUCTION

The measurement of regional bone metabolism is important for understanding bone physiology,[1] measuring response to treatment in early phase clinical trials of novel drugs to avoid late-stage attrition, and diagnosing patients in clinics with bone metabolic and metastatic diseases.[2–7] Bone histomorphometry

following bone biopsy is considered the gold standard method of measuring bone metabolism. However, it is limited to a single site, that is, the iliac crest, which is relatively painful and invasive for patients, and is a costly and complex technique subject to significant measurement errors.[8–12] An alternative method of measuring biochemical markers of bone formation or bone resorption in serum or urine provides a noninvasive measurement of bone metabolism. However, bone markers measure only global skeletal bone turnover, while it is recognized that there is significant heterogeneity with regard to skeletal physiology and pathology.[13,14] In particular, bone markers cannot provide information about specific sites, such as the hip and spine, that may be particularly susceptible to osteoporotic fractures.[15–18]

An alternative method of measuring bone metabolism is using positron emission tomography (PET) imaging to measure the metabolic flux (K_i, sometimes referred to as bone plasma clearance, units: ml/min/ml) of the bone-seeking tracer [^{18}F] sodium fluoride ([^{18}F]NaF). The [^{18}F] ion is an excellent bone imaging tracer extracted by the skeletal system in proportion to bone blood flow and bone metabolism at the sites of newly formed bone.[19] The ionic exchange of the fluoride happens with hydroxyl groups in hydroxyapatite crystals on the surface of newly formed bone matrix to form fluorapatite preferentially at sites of osteoblastic and osteoclastic activity and the newly mineralizing bone.[20–22] The [^{18}F]NaF PET method has been validated against the gold standard of bone biopsy.[23,24] The attraction of [^{18}F]NaF PET is that it allows the measurement of regional bone metabolism at one or more sites in the skeleton non-invasively from a single injection of the tracer.[25,26] The technique can measure changes in bone metabolism within weeks of the commencement of treatment, much earlier than changes in bone mineral density can be measured using dual-energy X-ray absorptiometry, which may take two or three years to detect.[27] Therefore, it has the potential to be a valuable imaging biomarker of response for utilization in clinical trials for early assessment of therapeutic efficacy.[28]

There are two main approaches to measuring bone metabolism using [^{18}F]NaF PET imaging, namely the measurement of standardized uptake values (SUV) and methods that measure K_i.[29,30] SUV is a semiquantitative measurement obtained from a static PET image usually acquired around 45–60 min after tracer injection. SUV is equal to the tracer concentration (units: Bq/ml) measured within the PET scan image volume of interest (VOI) divided by the injected tracer (units: Bq) per unit body weight of the patient (units: g). Therefore, SUV has units of g/ml, or effectively a dimensionless number assuming a mean body density of 1 g/ml. The measurement of SUV is popular due to its simplicity, lack of requirement for an AIF and precision error of around 10%, compared to the relative complexity of obtaining

K_i values with their larger precision error of typically 11%–15%.[31] Conventionally, the measurement of K_i is obtained from a combination of a 60-min dynamic scan and arterial or venous blood samples to enable the estimation of the metabolic flux. The standard mathematical model of [^{18}F]NaF bone tracer kinetics is the Hawkins model (Figure 1).

The two inputs to the model are the bone time-activity curve (TAC) obtained from the dynamic PET images and the arterial input function (AIF) describing the time-activity curve for the delivery of [^{18}F]NaF tracer to bone. From the bone TAC and AIF curves, the Hawkins model can be solved to derive between three and five parameters (K_1, k_2, k_3, k_4, and F_{BV}; for the definition of these parameters, see Figure 1 and its legend) using a computer program that matches the individual TACs for the bone mineral and bone ECF compartments to the measured TAC (Figure 2).

The parameters K_1, k_2 and k_3 are then used to derive the bone metabolic flux, K_i, from the equation:

$$K_i = K_1 \times \frac{k_3}{(k_2 + k_3)} \tag{1}$$

A simpler graphical method, referred to as the Patlak plot method, that avoids the need to derive the Hawkins model parameters will be described later in Section 5.3.[32] It is important to note that even simplified methods of measuring K_i with potential for translation to the clinic still require derivation of the AIF for individual subjects.[25,26]

Many researchers have presented various different static and dynamic methods of quantifying bone metabolism.[33–35] The advantage of measuring changes in bone metabolism using K_i rather than SUV is in situations where the disease processes involved have such a powerful effect on the whole skeleton uptake of [^{18}F]NaF tracer that the AIF is substantially altered from the curve typical of a healthy individual. This can occur in studies of disease progression, response to treatment, or comparing different cohorts with and without metabolic or metastatic bone diseases. In such circumstances, SUV measurements can give a false impression of true regional change, which may adversely impact the diagnosis or the measurement of response to treatment.[1,19,36–38] Therefore, in this review, we aim to discuss in particular the various methods of obtaining the AIF curve required for the measurement of bone metabolic flux in humans.

2 ┃ CALIBRATION

A calibration factor (CF) between the PET scanner and a gamma well-counter is required to convert the radioactive counts per minute obtained from the blood samples taken from the patient during the [^{18}F]NaF study into

FIGURE 1 This figure shows different versions of the Hawkins model used in the literature. K_1 and k_2 represent the forward and backward tracer exchange rates between blood and extracellular fluid (ECF), k_3 and k_4 represent the forward and backward tracer exchange rates between bone ECF and bone mineral, and F_{BV} is the fractional blood volume within the bone volume of interest. K_1 (units: ml/min/ml) is widely regarded as a measurement of bone blood flow. (a) Without any backflow of tracer from bone mineral to ECF (i.e., $k_4 = 0$); (b) With a non-zero value of k_4; (c) With a non-zero value of k_4 and allowing for a fractional blood volume F_{BV} within the skeletal region of interest. K_1 is widely regarded as a measurement of bone blood flow and is capitalized to denote it is measured in units of ml/min/ml. A lowercase k is used for k_2, k_3, and k_4 to denote that they are measured in units of min^{-1}.
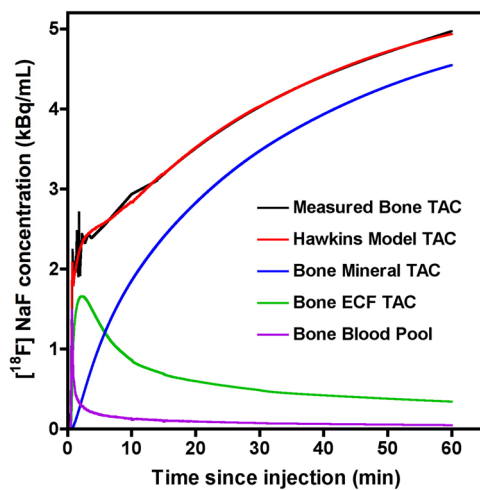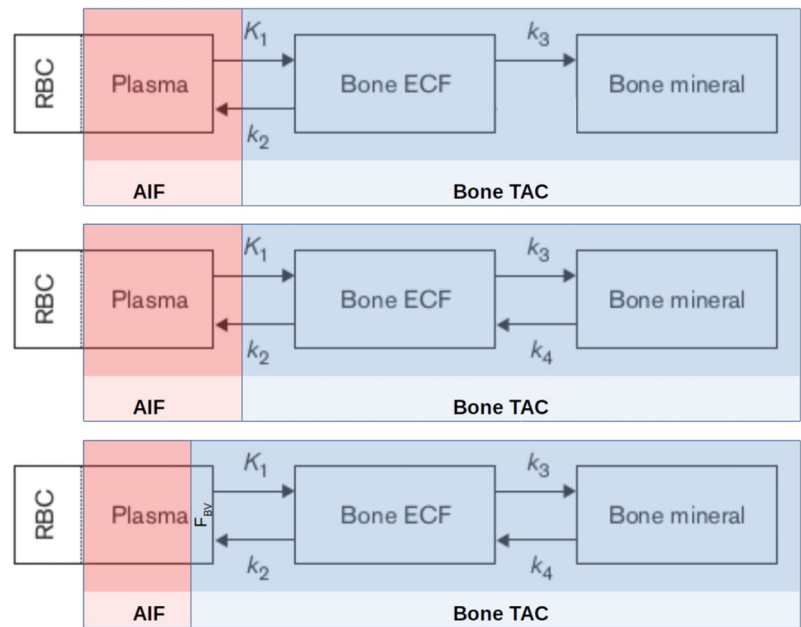
FIGURE 2 The output obtained from the mathematical modeling of bone time-activity curve and arterial input function using the Hawkins model and non-linear regression.

equivalent imaging units of Bq/ml. The CF is obtained by scanning a uniform cylinder phantom filled with ^{18}F solution for 5 min in the PET scanner and followed by counting a 0.2 ml aliquot in a well-counter for 5 min. At our center, the calibration factor is then calculated as follows:

$$CF = \frac{\text{PET scanner measurement (Units:Bq/ml)}}{[\text{Well } counter \, counts/60]\,/0.2 \,(\text{Units:counts/s/ml})} \quad (2)$$

In Equation 2, the well-counter measurement in units of counts per minute is divided by 60 to convert it into counts per second (s), and the measurement of counts/s

per 0.2 ml of aliquot is divided by 0.2 to convert it into counts/s/ml of aliquot. The PET image voxel values have units Bq/ml, where becquerel (Bq) is the unit for the quantitative measure of radioactivity defined as the number of nuclear decays occurring in a given quantity of material per second (i.e., counts per s). The CF has units: $\frac{\text{Bq/ml}}{\text{counts/s/ml}}$, or by substituting Bq with counts/s in the numerator, CF can be obtained as a unitless number. At our PET center, the calibration factor in Equation 2 is re-measured every 3 months.

Another consideration over the choice of units for time in seconds is that the direct arterial sampling study (that is the basis of our definition of our semi-population input function) generated blood concentration measurements at 1-s intervals. For this reason, to avoid any confusion at our center, we chose to do our calculations with time consistently in units of seconds and then, as the last step, convert our K_i values from units of ml/s/ml to ml/min/ ml. We also note that other centers may prefer to keep the well-counter measurement in Equation 2 in units of counts min^{-1} ml^{-1}. The difference is immaterial as long as care is taken with the units of time to ensure that the final result for K_i is in units of ml/min/ml.

3 | IMAGING PROTOCOL FOR A DYNAMIC [^{18}F]NaF STUDY

The United Kingdom Administration of Radioactive Substances Advisory Committee (ARSAC) guidelines list an effective dose to patients of 4.3 mSv following an injected activity of 250 MBq of [^{18}F]NaF intravenously administered for PET bone imaging.[39] This corresponds
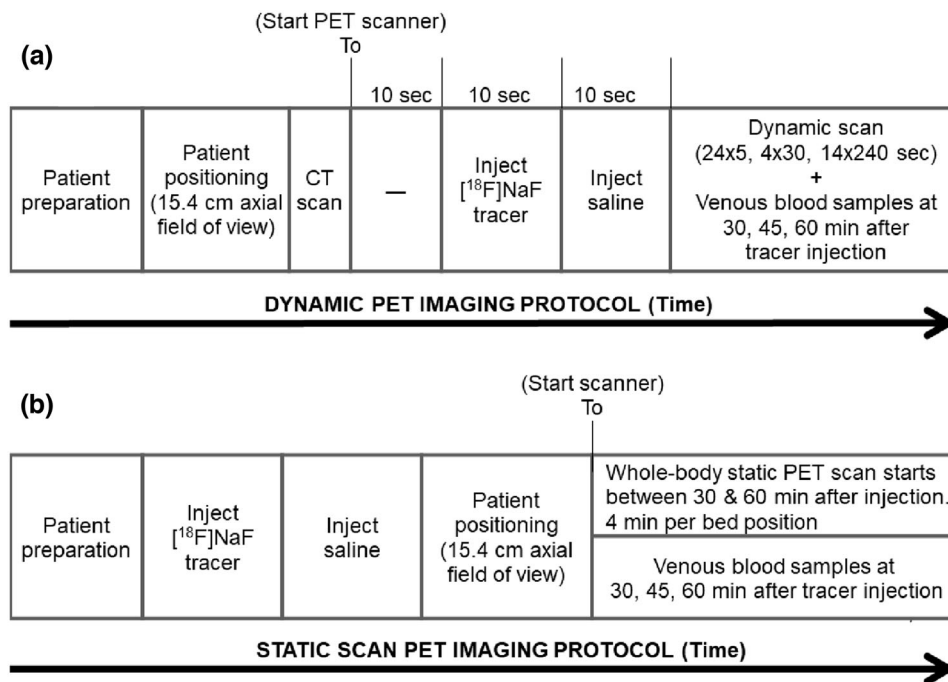
FIGURE 3 Imaging protocol used to obtain bone metabolic flux (K_i) values using: (a) a 60-min dynamic positron emission tomography (PET) scan; (b) a static PET scan protocol. It is important to note that a single bed position can be acquired with a 4 min static scan. At our center, we normally use two bed positions to acquire data associated with lumbar spines L1-L4. For reliable estimates of K_i values, we recommend that this static 4 min scan be performed between 30 and 60 min post tracer injection.[25]

to an effective dose of 1.72×10^{-11} Sv/Bq, which is consistent with the dose reported in the International Commission on Radiological Protection (ICRP) Publication 128.[40] The effective dose estimate depends on many factors, including assumptions made about organ uptake and biological half-lives, and the position and sizes of organs assumed for a healthy reference 35-year-old human male weighing 73 kg with a height of 176 cm and for a healthy reference 35-year-old human female weighing 60 kg. It should be noted that additional doses may be delivered to the patient from other procedures, for example, the computed tomography (CT) part of the PET-CT scan, which will vary depending on the tube current and CT scan time. Studies have shown that it is possible to obtain a successful quantitative [^{18}F]NaF PET scan at the lumbar spine using an injected activity as low as 90 MBq,[13,14] and some researchers have proposed further dose reduction strategies in preclinical settings.[41] However, radiation dosimetry is a field in itself, and this topic will not be discussed here any further.

Figure 3a shows a typical dynamic PET-CT scan protocol. Participants are asked to relax and keep well hydrated, which helps minimise the reabsorption of [^{18}F]NaF in the kidneys that may otherwise vary with urine flow rate. Patients are asked to empty their bladder immediately before the start of scan acquisition. Patients are positioned supine to cover the target VOI, for example, hip or spine, within the field of view (FOV) of the PET scanner (which is approximately 15 cm and

varies between different manufacturers, although total-body PET scanning has recently been introduced[42,43]). A CT scan is performed first, followed by an intravenous injection of [^{18}F]NaF at the start of the dynamic PET scan. The tracer is administered beginning 10 s after the start of scan acquisition and injected over a period of 10 s. This is followed by the injection of a 10 ml saline flush starting at t = 20 s and injected over a further 10 s. The images are acquired in list mode, along with the collection of the required venous blood samples.[19,26]

A portion of each whole blood sample is centrifuged to separate plasma and blood cells. The radioactivity counts rates (units: background-corrected counts/min (CCPM)) in plasma and whole blood are then measured using a well-counter and converted to the PET image voxel units of Bq/ml by applying the following correction factors:

$$\left(\frac{CCPM}{60}\right) \times (DWC) \times (CF) \times (DF)$$

where: CCPM/60 provides background-corrected counts/s; DWC is the density (units: g/ml) correction of the plasma or whole blood sample; CF is the calibration factor in units: $\frac{Bq/ml}{cts/s/ml}$; and DF is the decay factor which is dimensionless. The combination of all four correction factors converts the well-counter measurement units in CCPM into PET image voxel

units in Bq/ml as follows:

$$\left(\frac{cts/s}{1}\right) \times \left(\frac{g/ml}{g}\right) \times \left(\frac{Bq/ml}{cts/s/ml}\right) \times (1) = Bq/ml$$

For increased accuracy of the well-counter measurements of plasma and whole blood concentrations, it is recommended to weigh counting tubes before and after pipetting and convert weights to volumes using densities of 1.035 g/cm^3 for plasma and 1.057 g/cm^3 for whole blood.[44] The ratios of plasma to whole blood tracer concentrations over time are measured and used to correct the arterial whole blood tracer concentration curve to obtain the plasma concentration curve. The bolus peak within the plasma tracer concentration curve is then matched in time to the bolus peak observed on the bone TAC derived by placing a VOI on the dynamic PET image to derive the plasma AIF.

It is important to note that the injected dose and all tracer concentration values (from blood samples or images) have to be corrected back to a single reference time point to allow correction for radioactive decay. This is often chosen as the tracer injection time. However, in practice, any time can be chosen as the reference time (for example, the time when the tracer is drawn up in a syringe), provided that consistency is maintained.

The residual activity left over in the injection syringe is also measured, decay corrected back to the reference time, and then subtracted from the injected activity value measured before tracer administration to calculate the true injected dose to the patient accurately. Further details of the timing information required are shown in a flow chart (Figure S1), PET data collection sheet (Figure S2) and an Excel file (**"Supplemental File – Static scan Ki calculation.xlsx"**) in the Supplement section. The data include the amount of radioactivity measured, the time at which radioactivity is measured, the time of radioactivity injection to patient, residual activity left in the syringe, residual activity measurement time, the scanner start time and the times the blood samples are measured in the well counter. Since [^{18}F]NaF tracer does not metabolize or show protein binding, the AIF does not require metabolite correction to obtain the TAC of the parent plasma tracer concentration.[45]

The dynamic PET images are re-binned at different frame durations during image reconstruction, along with corrections for scatter events, random events, dead time and attenuation using the CT scan.[46] This allows the early phase of the dynamic study to be resampled in short time frames where the tracer concentration is rapidly changing to obtain an accurate image-derived AIF and allow the additional measurement of bone blood flow (K$_1$, units: ml/min/ml) using the Hawkins model (Figure 1). The later phase of the dynamic study, where tracer concentration is not rapidly changing, is resampled in longer time frames to obtain the bone TAC.

Ordered subset expectation maximization (OSEM) or filtered back projection (FBP) methods in two or three-dimensional (2D or 3D) mode can be used for image reconstruction, even though there may be some quantitative differences between the K$_i$ results obtained from images reconstructed using these two methods.[47] Even though reconstruction in 3D mode has been shown to be superior to 2D mode for various reasons based on noise equivalent counts (NEC),[48–51] it may be noted that the variation in count sensitivity is high in 3D mode and can vary strongly across the FOV,[52] which implies that the same activity concentration placed at the center of the FOV versus at the edge of FOV may give a different image pixel value. On the other hand, the sensitivity is lower in 2D but is almost constant throughout the FOV. Therefore, it is possible that 2D may be better for quantification and 3D may be better for visualization, and care should be taken when images are obtained and used for quantification.

4 | MODEL INPUTS

The two inputs required for modeling tracer kinetic using the Hawkins model[30] or Patlak graphical analysis[32] are the time variation of the mean tracer concentration in the target bone volume (i.e., the bone TAC) and the time variation of the tracer concentration in plasma in the artery feeding the target bone volume (i.e., the AIF).

Bone TAC: The bone TAC is the concentration of tracer within the target VOI measured over time and can be obtained in various ways. The region can be drawn manually or semi-automatically directly on a late frame of the dynamic PET image, and then the same region is transferred onto each dynamic PET frame to get a measure of tracer concentration in Bq/ml from the same spatial region in each frame.[53] Another way is to use the CT part of the PET-CT study to segment the bone regions on CT, and then the same region is transferred onto each time frame to measure tracer concentration from the same spatial region in each frame. For a lumbar spine study, the VOIs should be drawn wholly within the trabecular bone of the L1, L2, L3, and L4 vertebral bodies such that the VOI includes only the trabecular spongiosa of the vertebral bodies and the cortical bone surrounding the vertebral bodies is excluded. Typically, regions of interest in each vertebra can be drawn in three or four transaxial planes avoiding the endplates to construct the vertebral body VOI. The final results for K$_i$ or SUV are the average of all four vertebrae. Examples of coronal views at the lumbar spine and proximal femur visualized on static PET images are shown in Figures 4a and 4c, respectively. A transaxial view at the lumbar spine visualized as fused static PET-CT images with superimposed trabecular spongiosa region of interest (ROI) is shown in Figure 4b. Figure 4d shows an example of a transaxial view of a lumbar spine dynamic PET scan visualized
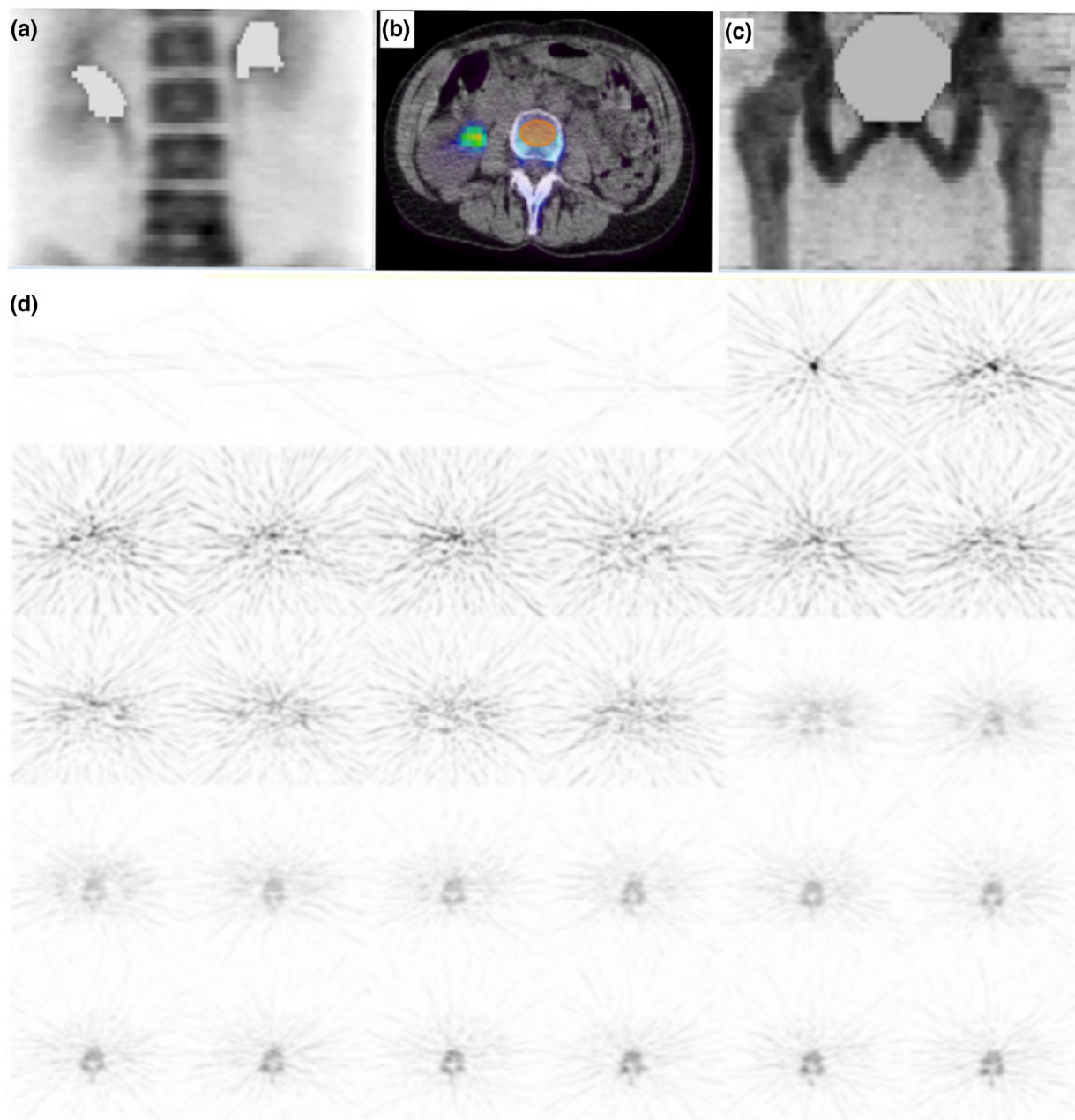
FIGURE 4 (a) Example of a coronal view of the lumbar spine (LS) on a PET image; (b) Example of transaxial view of the LS on a PET-CT fused image with a region of interest (ROI) used to measure K$_i$ shown with an orange color that includes only the trabecular spongiosa of the vertebral bodies and excludes the cortical bone surrounding the vertebral bodies; (c) Example of a coronal view of the proximal femur on a PET image. The high activity accumulations in the kidneys and the bladder have been removed for a clearer presentation of the images. (d) Example of a dynamic [^{18}F] NaF PET scan showing a single transaxial slice at the lumbar spine over multiple time-frames from 0 to 60 min after tracer injection.

over multiple time frames from 0 to 60 min after tracer injection.

AIF: The AIF is the concentration of tracer within the artery supplying the blood to the skeletal VOI. Conventionally, the [^{18}F]NaF concentration in arterial plasma is used rather than the concentration in whole blood. The AIF can be obtained in various ways, for example, by continuous arterial blood sampling,[54] venous sampling starting at early time points after warming the hands to 43°C (arterialized blood),[55,56] or using venous blood samples obtained between 30 and 60 min post-injection (by which time the arterial and venous concentrations have equalised[54]) to calibrate image-derived time–activity curves of the blood,[57,58] or by using a semi-population input function that combines individual measurements of venous blood samples obtained between 30 and 60 min to define the terminal exponential with a population derived residual curve to model the

early fast exponentials.[59] For some methods of deriving the plasma AIF, for example, direct arterial sampling and image-derived AIF, it is necessary to use venous blood samples to measure the plasma-to-whole blood ratio. The whole blood AIF calibrated against these samples is then corrected to obtain the plasma AIF that is used for modeling. Since it is assumed that arterial tracer concentration is the same throughout the blood in the body due to homogeneous mixing, it can be measured in any peripheral artery. However, to avoid the risk of contamination from the injection site, venous blood samples should not be taken from the same arm used to inject the tracer. The different methods used to measure the AIF are described in more detail in the following sections.

4.1 | Direct arterial sampling

Direct arterial sampling is the most complete and accurate method of measuring the AIF. However, it is relatively complicated and invasive, and the insertion of the arterial catheter requires the assistance of an anesthetist.

Since the arterial concentration of [^{18}F]NaF varies rapidly during the first few minutes after tracer injection and does not reach equilibrium with the venous concentration until around 30 min, the AIF during this period is most accurately measured by continuous direct sampling from the radial artery. For example, Cook et al.[54] used an automated online blood sampling system (Allog AB, Mariefred, Sweden) with 1 m long polyethylene tubing, a 1 mm internal diameter, and a flow rate of 5 ml min^{-1} to continuously measure the AIF in ten subjects undergoing dynamic [^{18}F]NaF PET imaging. The continuous whole blood counts from the artery were calibrated with a series of six discrete arterial samples taken at 5 min intervals during the 30 min measurement period. A three-way tap placed downstream from the detector at the distal end of the radial artery line was used for discrete sampling. Venous blood samples were also taken at 2, 4, and 10 min and then every 10 min until the end of the PET scan at 60 min. The blood samples were centrifuged, gamma counts were measured in plasma and whole blood in a gamma-counter, and these counts were converted to imaging units, as described in the previous section. The plasma-to-whole blood ratio is either constant or very slowly varying over a 60-min dynamic scan. Calibrated measurements from the continuous online blood sampling system are corrected for the plasma to whole blood ratio using a linear regression fit to the blood ratio data.

4.2 | Semi-population method (SP-AIF)

The 0−60 min SP-AIF proposed by Blake et al.[59] has two parts: (1) a single exponential (described as the
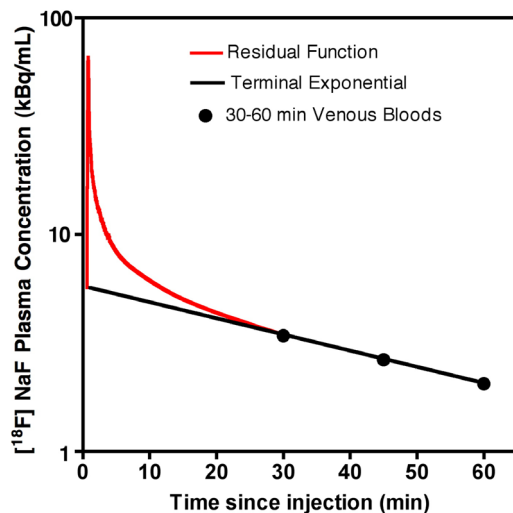

FIGURE 5 Figure explaining the semi-population arterial input function (SP-AIF). Note the logarithmic scale on the vertical axis. The terminal exponential (0-3600 s) is shown in black and is generated from venous blood samples taken from the individual patient between 30 and 60 min after the tracer injection. By this time venous and arterial blood concentrations of [^{18}F] NaF tracer are in equilibrium and are equal. A single exponential has been fitted to the three blood points shown in the figure and extrapolated back to t = 0. The red curve shows the residual function (0-1800 s), which is the population average of arterial data obtained from nine postmenopausal women by direct sampling. In each of these women, her individual residual function was obtained after subtracting her terminal exponential and scaling to an injected activity of 100 MBq. The red curve is the average residual function for the nine women. In clinical studies, the SP-AIF is constructed by adding the population-based residual function to the individual patient's terminal exponential after scaling the residual function for injected activity.

"terminal" exponential) fitted to venous blood samples obtained at 30, 45, and 60 min after tracer injection and extrapolated back to the time of injection; (2) a residual function representing the sum of the early fast exponentials between 0 and 30 min that is added to the terminal exponential to produce the complete AIF (Figure 5).

The venous blood samples are measured individually in each patient, while the residual function is a population average curve that is scaled by the injected activity in each individual patient. The residual function is the average of nine of the ten postmenopausal women studied by Cook et al.[54] (one woman was excluded because the arterial blood sampling finished at 20 min). In each of the nine women, the terminal exponential fitted to the 30−60 min venous blood samples was subtracted from the calibrated arterial measurements at 1-s intervals to derive the residual function. The nine residual functions were then normalized to an injected activity of 100 MBq, and time adjustments were applied to bring their peaks into coincidence before averaging the nine curves to derive the 0−1800 s population residual curve (Figure 6).

A mathematical function that accurately reproduces this curve in units of kBq/ml in three separate time
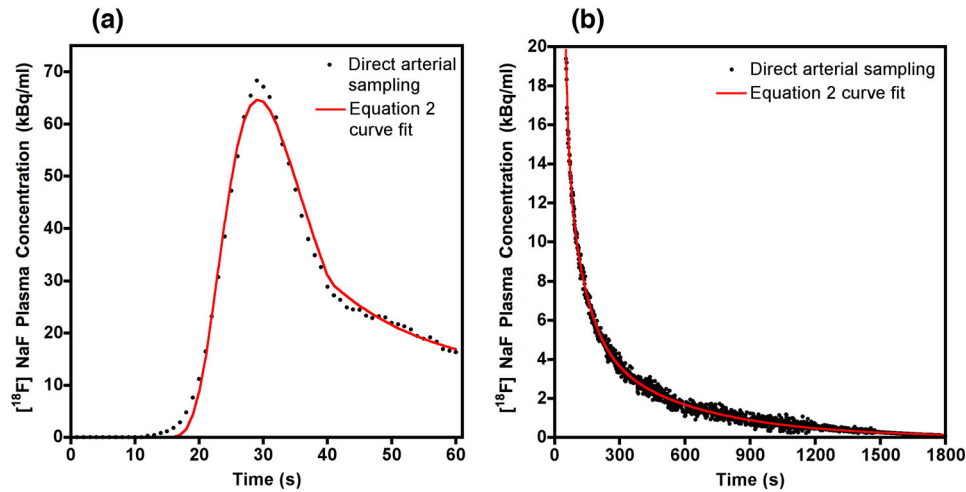
FIGURE 6 Plots of the population mean arterial plasma concentration residual curve at 1-s intervals obtained from direct arterial sampling in nine postmenopausal women and normalized to 100 MBq of injected activity. (a) The residual curve between 0 and 60 s; (b) The curve between 60 and 1800 s. Black dots show the average data points from the nine women, and the red curve shows the curve fit (see Equation 3) plotted on top for comparison. The timing of each of the nine curves obtained by direct arterial sampling was adjusted to ensure the peak counts occurred exactly 30 s after injection.

intervals is presented in Equation 3:

$$[1]\ SP - AIF(t) = 0,\ \text{for}\ 0 < t < 12s$$
$$[2]\ SP - AIF(t) = (a \cdot t^b) \cdot \exp(c \cdot t^d),\ \text{for}\ 12 \leq t \leq 40s$$
where $a = 1.90968 \times 10^{13}$; $b = -7.06237$; $c = -26266$; $d = -2.73482$
$$[3]\ SP - AIF(t) = a \cdot \exp(b \cdot t) + c \cdot \exp(d \cdot t) + e \cdot \exp(f \cdot t),\ \text{for}\ 40 < t < 1800s$$
where $a = 280.81$; $b = -0.074670$; $c = 17.083$; $d = -0.01168$; $e = 5.9043$; $f = -0.0021085$

$$(3)$$

For an injected activity of 100 MBq, the area under the plasma curve (AUC) of Equation 3 is 4560 kBq s/ml (76.0 kBq min/ml) compared with 4569 kBq s/ml (76.15 kBq min/ml) for the original raw data. To generate a 0−60 min SP-AIF in an individual patient, the population residual curve between 0 and 30 min is scaled to the injected activity to that patient and added to the single exponential curve fitted to the venous plasma concentrations measured at time points between 30 and 60 min post-tracer injection (Figure 5).

The terminal exponential fitted to the venous plasma measurements accounts for typically 75−80% of the total area under the 0−60 min AIF curve, so the method accounts for the majority of the real differences in 0−60 min AUC between patients required for the estimation of K_i values. When applied to clinical research studies investigating treatment response in osteoporosis patients, the SP-AIF method assumes that the response to treatment alters the terminal exponential of the AIF and has a negligible effect on the bolus peak and early fast exponential terms that mainly reflect the rapid early flow of tracer from the circulation into soft tissue.[25,26,60,61] Therefore, the values of K_i obtained using the SP-AIF method may differ slightly from the K_i values obtained using direct arterial sampling. A limitation of Equation 3 is that it was derived from a small group of postmenopausal white women and may not be applicable in other populations. Also, using the SP-AIF is inappropriate for calculating bone blood flow (K_1) values as it uses the population average value for the bolus peak and may not reflect how the tracer concentration changes within an individual patient during the first few minutes after the tracer injection. Since accurate measurement of K_1 values depends on knowing the plasma tracer concentration in the supplying artery during the first 2−3 min after tracer injection, accurate estimates of K_1 require either direct arterial sampling or the measurement of an image-derived input function (ID-AIF) obtained by placing a VOI within the dynamic PET image to obtain the arterial blood TAC corrected for partial volume and spill-in effects.

An important advantage of the SP-AIF method is that it allows the measurement of K_i values at multiple skeletal sites from a sequence of short (typically 4 min) static scans acquired at multiple bed positions using a single tracer injection during a single scan session (Figure 4a,c). When the SP-AIF method was compared to other input function methods, for example, the fixed partial volume correction (PVC) method,[57,58] the variable PVC method,[57,58] or the methods of Chen et al.[62] and Cook et al.,[54] in terms of the precision errors of the K_i values obtained using the Hawkins compartmental model or the Patlak graphical method, the SP-AIF showed the best performance (i.e., the lowest precision errors).

The use of the SP-AIF method was also investigated by Vrist et al. in a paper that compared K_i values derived from dynamic and static [¹⁸F]NaF PET scans acquired in patients with chronic kidney disease mineral and

bone disorder (CKD-MBD).[63] Their study differed from that of Blake et al. in that the gold standard AIF data used to calibrate the residual function was derived by imaging the left ventricle instead of direct arterial sampling. Their method differs in that the residual function is used to multiply the terminal exponential rather than added to it and therefore takes a value of exactly 1.0 at times ≥ 30 min after injection. A potential advantage of the multiplicative method is that it might allow for variation of the AIF with body size. In contrast, an additive residual function might be more appropriate in situations where the terminal exponential changes during a study due either to the extent of metabolic or metastatic bone disease or the use of treatments with a potent effect on bone metabolism. Vrist et al. concluded that the K_i values measured using either an SP-AIF or an image-derived AIF correlate well, and that the combination of the SP-AIF method with one or more static scans markedly reduces overall study times.

4.3 | Image-derived arterial input function (ID-AIF)

An ID-AIF is obtained by placing a VOI over a feeding artery within the FOV of the dynamic PET image and correcting for the partial volume effect (due to the limited spatial resolution of the scanner compared to the size of the artery), and spill-in effects (due to the tracer concentration in the surrounding tissue).[64,65]

In general, the VOI is drawn over 3−6 transaxial slices where the bolus activity is best visualized within the feeding artery on a dynamic image.[57,58] The same VOI is copied to all PET time frames, and a measure of tracer concentration in image voxel units (Bq/ml) is obtained and plotted against time. This 0−60 min blood TAC obtained in this way is labeled IMG(t). Another VOI placed in adjacent tissue giving the background TAC obtained from the dynamic image is labelled B(t). C(t) is the whole blood tracer concentration obtained by measuring the tracer counts (counts/min) in a well-counter from the venous blood samples obtained during the dynamic PET scan every 10 min between 30 and 60 min after tracer injection, which is then converted into PET image voxel units (Bq/ml) using the four factors described in the previous section.

The blood data at 30−60 min is resampled at PET image frame times, and a single exponential is fitted before further processing. The values of IMG(t = 30-60min), C(t = 30-60min) and B(t = 30-60min) at the image frame times are then substituted into Equation 4 as follows:

$$IMG(t) = \alpha \cdot C(t) + \beta \cdot B(t) \tag{4}$$

to obtain the values of α and β, where α is the partial volume correction (PVC) factor, and β is the spill-in fraction of background activity mixed with the arterial signal. Once the values of α and β are obtained by minimizing the differences between the left-hand side and right-hand side of the equation without any constraints applied on their values, these values are substituted back into the equation along with IMG(t = 0-60min) and B(t = 0-60min) to obtain C(t = 0-60min), and then re-sampled at 1 s intervals to obtain the ID-AIF. The model in Equation 4 assumes that the tracer concentration values measured on the PET scan image in the whole blood are equal to a linear combination of the true arterial whole blood concentration underestimated by a factor α due to the PVC, and a spilled-in activity concentration a factor β of the background tissue concentration. This method of measuring the ID-AIF by deriving an individual value of the PVC factor for each subject is referred to as the variable PVC method.

Since the [^{18}F]NaF concentration is higher in plasma than whole blood and the PET images measure whole blood, the C(t = 0-60min) function requires a correction for the plasma-to-whole blood ratio similar to the direct arterial sampling method. The plasma and whole blood tracer concentrations are first obtained from the venous blood samples obtained at 30−60 min post tracer injection from the patient during the dynamic PET scan. In general, the plasma-to-whole blood ratio shows little variation with time after injection, but if necessary, the ratios between 30 and 60 min can be fitted by linear regression, and the fit extrapolated to obtain the plasma-to-whole blood ratios between the 0−60 min resampled at 1 s intervals. The C(t = 0-60min) curve is then multiplied by the plasma-to-whole blood ratios between 0 and 60 min to obtain the plasma ID-AIF between 0 and 60 min.

One variation of this method is when the α value in Equation (4) is fixed by using the population average value to obtain the ID-AIF, referred to as the fixed PVC method. The second variation of this method is that proposed by Chen et al.[62] originally for brain imaging using [^{18}F]FDG scans and further explored by Puri et al.[57,58] for bone imaging using [^{18}F]NaF tracer. The only difference with the Chen et al.[62] approach is that they used a non-negative linear least-squares fitting approach to minimize the differences between the left-hand and right-hand side of Equation 4 such that the values of α and β are constrained to lie between zero and unity. The third variation of this method is that proposed by Cook et al.,[54] which assumes that the sum of α and β (in Equation 4) is equal to unity.

The typical diameter of the femoral artery in 65-year-old women has been reported as 8.8 ± 1.6 mm, and the diameter of the aorta as 21.8 ± 3.6 mm. The mean value of α obtained by Puri et al.[57,58] for the fixed and variable PVC methods at the femoral artery was 0.68
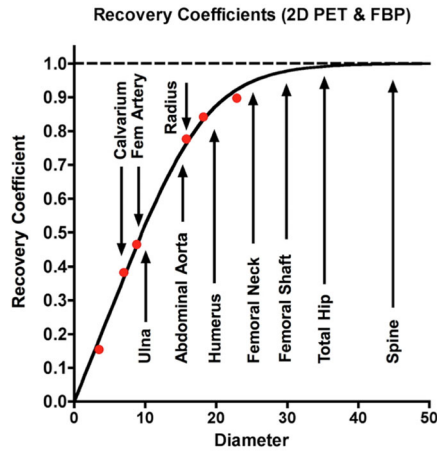
FIGURE 7 Figure showing the recovery coefficients, that is, the ratios of true activity concentrations and those measured from the phantom images, reconstructed using the same parameters (two-dimensional mode and filtered back-projection algorithm) as those used for PET imaging in our studies.

and 0.73 and at the aorta was 0.76 and 0.76, respectively. When these values of PVC were compared with those obtained with a phantom (Figure 7) using the same image reconstruction parameters as those used for the dynamic PET images,[66] the α values obtained at the aorta are consistent with the phantom. However, for the diameter of the femoral artery, the phantom values in Figure 7 suggest an α value close to 0.45.

5 | MATHEMATICAL MODELING

A number of different methods have been compared for modeling the bone metabolic flux K_i value, including different variations of the Hawkins model with or without setting $k_4 = 0$ and with or without the inclusion of the fractional blood volume (F_{BV}) in the skeletal region of interest (Figure 1); deconvolution analysis; spectral analysis; and Patlak graphical analysis.[31,34] Even though the Hawkins and Patlak models are popular, these methods have been extended by Siddique et al.[25] to estimate K_i at multiple sites from a series of one or more 4-min static scans, and by Puri et al.[26] to obtain both K_1 and K_i at a single site from a dynamic scan as short as 12 min. Here we will briefly describe four examples: (a) a simple version of the Hawkins model that includes k_4 but not the fractional blood volume inside the skeletal region of interest (Figure 1b); (b) the short dynamic scan method[26]; (c) the Patlak method; and (d) the 4-min static scan method.[25]

5.1 | The 60-min dynamic scan method

The changes in tracer concentration in bone mineral (C_b) and bone extracellular fluid (ECF) (C_e) are repre-

sented using Equations 5 and 6 based on the Hawkins model (Figure 1b):

$$\frac{dC_b(t)}{dt} = k_3 \cdot C_e(t) - k_4 \cdot C_b(t) \quad (5)$$

$$\frac{dC_e(t)}{dt} = K_1 \cdot C_p(t) - (k_2 - k_3) \cdot C_e(t) + k_4 \cdot C_b(t) \quad (6)$$

The solution to these differential equations can be obtained by solving these equations to obtain Equation 7, describing the tracer concentrations C_e and C_b over time.[52] It is important to note that C_p (representing the AIF) remains an important factor in these equations to obtain the K_i value

$$\begin{bmatrix} C_e \\ C_b \end{bmatrix} = \begin{bmatrix} C_p \otimes \left\{ K_1(\lambda_1 - \lambda_2)^{-1} \left[(k_4 + \lambda_1) e^{\lambda_1 t} - (k_4 + \lambda_2) e^{\lambda_2 t} \right] \right\} \\ C_p \otimes \left\{ K_1 k_3 (\lambda_1 - \lambda_2)^{-1} \left[e^{\lambda_1 t} - e^{\lambda_2 t} \right] \right\} \end{bmatrix} \quad (7)$$

where $\lambda_{1,2} = \frac{-(k_2+k_3+k_4) \pm \sqrt{(k_2+k_3+k_4)^2 - 4k_2 k_4}}{2}$ and the cross surrounded by a circle represents the convolution operator. Since the bone TAC obtained from placing an ROI over the PET image includes the concentration from C_e and C_b, the differences between the left-hand (from the PET image) and right-hand side (from the model) can be minimized using non-linear regression as represented in Equation 8:

$$C_t = C_b + C_e \quad (8)$$

to obtain the individual k-parameters, for example, K_1, k_2, k_3, and k_4. Then using the individual k-values, the K_i value is calculated using Equation 9:

$$K_i = K_1 \times \frac{k_3 \cdot C_e}{(k_2 + k_3) \cdot C_e} = K_1 \times \frac{k_3}{(k_2 + k_3)} \quad (9)$$

thus arriving at the result first presented in Equation 1.

A previous study by Jassel et al.[88] investigated the issue of whether bone K_i measurements could be normalized to the weight of bone mineral in each mL of bone tissue. Rather than assuming a general density for bone (~1.75 g/ml), they tried to normalize K_i values to the individual patient's quantitative CT (QCT) measurement of volumetric BMD expressed in Hounsfield units (or equivalently, a DXA measurement of bone mineral apparent density (BMAD)). However, at present, there is no convincing evidence to suggest that either of these choices provide an improved version of K_i values. One important point is that bone turnover is a process that takes place on bone surfaces. Hence, perhaps the normalization should be to the surface area of bone in each unit volume of the tissue rather than the mass. However, there is no way of directly measuring this.

It is important to note that the K_1 value obtained via the Hawkins model procedure provides a local measure of blood perfusion, as shown in Equation 10:

$$K_1 = E \cdot F \cdot (1 - PCV)$$
$$= \left(1 - e^{(-P \times S/F)}\right) \cdot F \cdot (1 - PCV) \quad (10)$$

Since the blood perfusion depends on the blood flow, and the product of capillary permeability and surface area, the first part of the K_1 equation is (1-exp(-P*S/F)), where P is the blood capillary permeability, S is the capillary surface-area, and F is the local blood flow. The term (1-exp(-P*S/F)) is sometimes referred to as the tracer extraction fraction (E) and approximates to 100% at low to moderate flow rates (i.e., less than or equal to 0.16 ml/min/ml).[67–70] The bone perfusion measured using [^{18}F]NaF is in good agreement with measurements made using [^{15}O]H$_2$O, the recognized gold standard for radionuclide blood flow studies.[69,70] The packed cell volume (PCV) is a way of converting blood flow into plasma flow and therefore relating blood flow to the K_1 measurement. It has no effect on the shape of the input function.

Equation 10 can be understood using a graph of Y = exp(-X); when the X-value increases, the corresponding Y-value decreases and becomes negligible. Therefore, a lower value of F in equation E = (1-exp(-P*S/F)) leads to a large value of P*S/F, and therefore, a negligibly small value of exp(-P*S/F), and hence, the value of E approaches unity.

5.2 | The short dynamic scan method

In the short dynamic scan method, the Hawkins model is solved using fixed population average values of k_2, k_3, k_4 and F_{BV}. By avoiding using freely fitted values of these parameters, the dynamic scan time can be shortened without losing any precision in the final K_i measurement. Puri et al. used Hawkins model solutions of 60-min dynamic scans with freely fitted parameters as the reference method against which the short dynamic scan method was compared.[26] Using fixed population average values of $k_2 = 0.194$, $k_3 = 0.187$, $k_4 = 0.014$ and $F_{BV} = 0.002$, they analyzed the bone TAC and the AIF to obtain the best fit value of K_1. K_i was then calculated using Equation 1. By fixing the values of four parameters in the Hawkins model, they obtained comparable values of K_i with similar statistical accuracy as the conventional 60-min dynamic scan method with scan times as short as 12 min. It is important to note that an accurate measurement of the AIF remains an essential factor to obtaining reliable values of K_i, preferably using the semi-population-based method. Another benefit of the short dynamic scan method is that for hip studies, it largely avoids the streaking artifacts and spill-in of activity from the accumulation of bladder activity that can invalidate measurements at sites such as the femoral neck in some patients.[47,56]

## 5.3 | The Patlak plot method

The Patlak plot method (Figure 8a) is based on the assumption that, once equilibrium is reached between the concentrations of tracer in plasma and the reversible bone ECF compartment in the Hawkins compartmental model (Figure 1), the rate of change of the tracer concentration in the irreversible bone compartment is directly proportional to the plasma concentration.[32]

This assumption is valid provided the value of k_4 is negligibly small (i.e., $k_4 = 0$). In practice, we obtain $k_4 = 0.01$ min^{-1} (approximately) from the Hawkins model with a corresponding half-life of 70 min, which is comparable to the 60-min dynamic scan that is generally performed for estimating K_i values in bones. However, the Patlak plot method can also be modified to allow for a non-zero value of k_4.[71] With the above two assumptions, the net concentration of tracer in the tissue ROI can be represented as the sum of the concentrations in bone ECF and bone mineral, and can be mathematically represented as follows:

$$\frac{C_{bone}(T)}{C_{plasma}(T)} = K_i \times \frac{\int_0^T C_{plasma}(t)\,dt}{C_{plasma}(T)} + V_o \quad (11)$$

where $C_{bone}(T)$ is the activity concentration of tracer (in units: Bq/ml) at any time T obtained from the PET image by placing a VOI in the skeletal region, $C_{plasma}(T)$ is the arterial plasma concentration of tracer (in units: Bq/ml) at time T, V_o is the effective distribution volume of the tracer in the bone ECF (the fraction of the total VOI occupied by the ECF compartment), and $\int_0^T C_{plasma}(t)dt$ is the area under the plasma AIF curve, which is the net tracer delivery to the tissue region of interest (in units: Bq s/ml) over the time interval between 0 and T. Equation 11 is a linear equation of the form Y = m*X + c, where $Y = \frac{C_{bone}(T)}{C_{plasma}(T)}$ is referred to as the normalized bone uptake and $X = \frac{\int_0^T C_{plasma}(t)dt}{C_{plasma}(T)}$ is referred to as the normalized time (FIGURE 8a). The data plotted on the Y- and X-axes between 10 and 60 min (because the nonlinear part during the non-equilibrium state of the system between 0−10 min is ignored) is fitted by linear regression to obtain the values of m and c, where m is the slope of the regression line representing K_i and c is the Y-intercept of the regression line representing the volume of distribution, V_o.

Figure 8b shows a scatter plot of values of K_i derived using the Patlak plot method against values derived
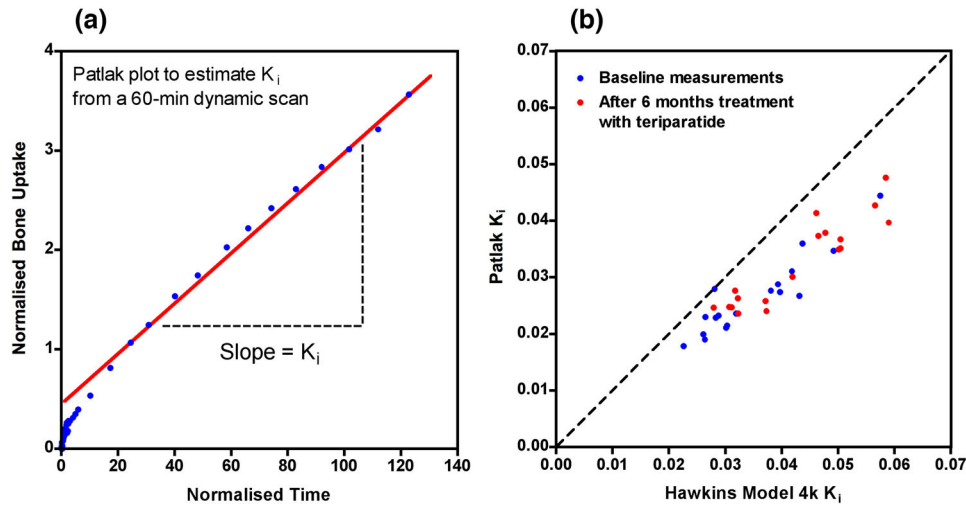
FIGURE 8 (a) Patlak graphical analysis of a 60-min [18F]NaF dynamic PET scan. Blue dots show the data from individual frames in the dynamic scan, and the red line is the linear regression fit to the last 13 data points obtained between 10 and 60 min after injection. The intercept of the linear regression line is the volume of distribution of the extracellular fluid (ECF) space, that is, the fraction of the PET scan bone volume of interest (VOI) occupied by ECF, also known as Vo. The value of K_i is obtained from the slope of the regression line. Normalized time $= \frac{\int_0^T C_{plasma}(t)dt}{C_{plasma}(T)}$; normalized bone uptake $= \frac{C_{bone}(T)}{C_{plasma}(T)}$, where T is the acquisition time of each individual frame of the dynamic scan, $C_{plasma}(T)$ is the [18F]NaF plasma concentration at time T, and $C_{bone}(T)$ is the bone concentration. (b) The scatter plot of K_i values derived using the Patlak plot method against values derived using the Hawkins model shown in Figure 1c that allows for a freely fitted value of k_4. The data is from a study of 18 postmenopausal women with low bone density (i.e., osteopenia) who were treated for six months with the parathyroid hormone (PTH) analog teriparatide. Blue points are the baseline measurements, and red points are those after six months of treatment. The Patlak values of K_i are systematically lower than the Hawkins model values by an average of 25% because of the assumption that $k_4 = 0$ in deriving the Patlak values.

using the Hawkins model shown in Figure 1c, that is, allowing for a freely fitted value of k_4. The data is from a study of 18 postmenopausal women with low bone density (i.e., osteopenia) who were treated for 6 months with the parathyroid hormone (PTH) analog teriparatide.[60] Both baseline (blue points) and 6-month follow-up data (red points) are plotted. The Patlak K_i values are systematically lower than the Hawkins model K_i values by an average of 25% because of the assumption that $k_4 = 0$ in deriving the Patlak K_i values. Much of the scatter in the differences between the Patlak and Hawkins model values of K_i reflects the random statistical errors in the Hawkins model derivations of k_4.[26]
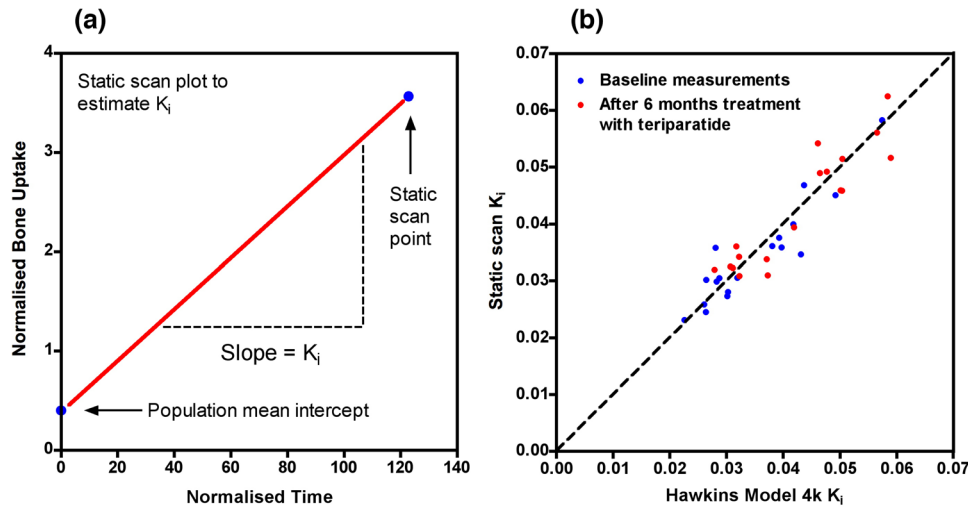
5.4 | The static scan method

Siddique et al.[25] showed that it is possible to measure K_i values using a short (4 min) static [18F]NaF PET scan acquired at times between 30 and 60 min after tracer injection. An imaging protocol for this method is summarized in Figure 3b. The static scan method uses a modified version of Patlak analysis[32] based on fitting a straight line to just two data points; the first point is a population average value of the Y-axis intercept on the Patlak plot (V_0), and the second point is a measurement of a single static scan image (Figure 9a). With the use of a fixed value of V_0, values of K_i can be calcu-

lated directly from Equation 11. By acquiring a series of static scans at different sites in the skeleton (say, the spine and hip), it is possible to measure K_i at multiple sites with a single injection of the tracer. The approach uses the SP-AIF with venous blood samples taken at 30, 45, and 60 min (Figure 3b). On the assumption that $k_4 = 0$, the authors derived the population average values of $V_0 = 0.46$ at the spine and 0.19 at the hip. They also found that V_0 did not change significantly during treatment with teriparatide.

In a subsequent publication, Siddique et al.[71] corrected the method to allow for efflux of tracer from bone equivalent to $k_4 = 0.012$ min^{-1}. On this basis, they found $V_0 = 0.22$ at the spine and 0.10 at the hip and concluded that, with the adjustment for the population average value of k_4, accurate values of K_i could be obtained with static scan times up to 90 min after injection. It was also noted that a 50% change in the V_0 value at the lumbar spine would cause only a 5% change in the K_i values at the lumbar spine for the clinical application in question.

Figure 9b shows a scatter plot of values of K_i derived using the static scan method against the values derived using the Hawkins model for the same study population as that shown in Figure 8b. The static scan K_i data were calculated to adjust for tracer efflux from bone.[71] With this correction, the points are scattered on either side of the line of identity. Hawkins model values of k_4 before and after treatment were poorly correlated (r = 0.28),

FIGURE 9 (a) Graphical explanation of how the static scan method is used to determine the value of K_i from the slope of the straight line fitting just two data points. The point at the lower left is the population mean volume of distribution of the bone extracellular fluid space (i.e., Vo) and the point at the upper right is the result from a single static scan acquired between 30 and 60 min after tracer injection. Normalized time $= \frac{\int_0^T C_{plasma}(t)dt}{C_{plasma}(T)}$; normalized bone uptake $= \frac{C_{bone}(T)}{C_{plasma}(T)}$, where T is the acquisition time of the static scan, $C_{plasma}(T)$ is the [^{18}F] NaF plasma concentration at time T, and $C_{bone}(T)$ is the bone concentration. (b) The scatter plot of values of K_i derived using the static scan method against the values derived using the Hawkins model for the same study population as that shown in Figure 8b. The static scan K_i data were calculated to adjust for the mean tracer efflux from bone (i.e., K-loss).[71] With this correction, the points are scattered on either side of the line of identity.

suggesting that much of the random scatter about the line of identity in Figure 9b can be explained by random statistical errors in the Hawkins model derivations of k_4.[26]

In their study of CKD-MBD patients, Vrist et al. concluded that both the dynamic and static scan methods were suitable for evaluating K_i, with the AIF derived either by dynamic imaging of the left ventricle or by using the SP-AIF method.[63] The simplified static graphical analysis was found to be preferable for implementation in clinical practice due to its short time scan and its ability to examine multiple bone regions using a single tracer injection, compared to the limitation of a single FOV with a dynamic scan acquisition. There was no systematic difference in the K_i results obtained by static scan analysis compared with a 60-min dynamic scan using the Hawkins model. We note that the static scan method should be applied with caution to other clinical areas using other tracers for other disease types where the relevant assumptions may not hold true.

5.5 | Calculation of K_i values

The Supplement section of this review includes a graphical explanation of how the Excel spreadsheet calculates K_i values (FIGURE S1) and a PET data collection sheet (FIGURE S2) used during image acquisition, and an Excel spreadsheet ("**Supplemental File – Static scan Ki calculation.xlsx**") for the calculation of SUV and K_i values using the static scan method together with notes on its use. There is also a flow chart explaining the spreadsheet. By entering the necessary time and activity data, the results are calculated automatically using Equation 11. The values of K_i given by this spreadsheet are those based on the assumption that $k_4 = 0$ and approximate to those obtained from a Patlak plot using dynamic scan data without the K-loss correction applied by Siddique et al.[71] We note that the spreadsheet allows the static scan method to be applied to the reanalysis of previously acquired dynamic [^{18}F]NaF PET data where venous blood data is also available. We hope that this SP-AIF model and the Excel spreadsheet will allow researchers to pool data from multiple centers across different institutes or countries and allow larger meta-analysis to be performed with clinically relevant hypotheses with higher statistical power (similar to genome-wide association studies), which may allow this technique to translate into the clinic for diagnostic purposes in the future.

For more complicated modeling using the Hawkins method, there is a plethora of commercial and non-commercial software, for example, MATLAB (The MathWorks, Inc., Natick, Massachusetts, USA), PMOD (PMOD Technologies Ltd., Zurich, Switzerland), Hermes Medical Solutions (Hermes Medical Solutions Ltd, Stockholm, Sweden), APPIAN,[72] QMODELING,[73] KINFITR,[74] AMIDE,[75] CARIMAS,[76] COMKAT,[77] KMTOOL,[78] or TKMF.[79] We hope that other new emerging clinical applications of [^{18}F] NaF PET[80–87] may also benefit from this review, especially from the SP-AIF model presented in Equation 3.
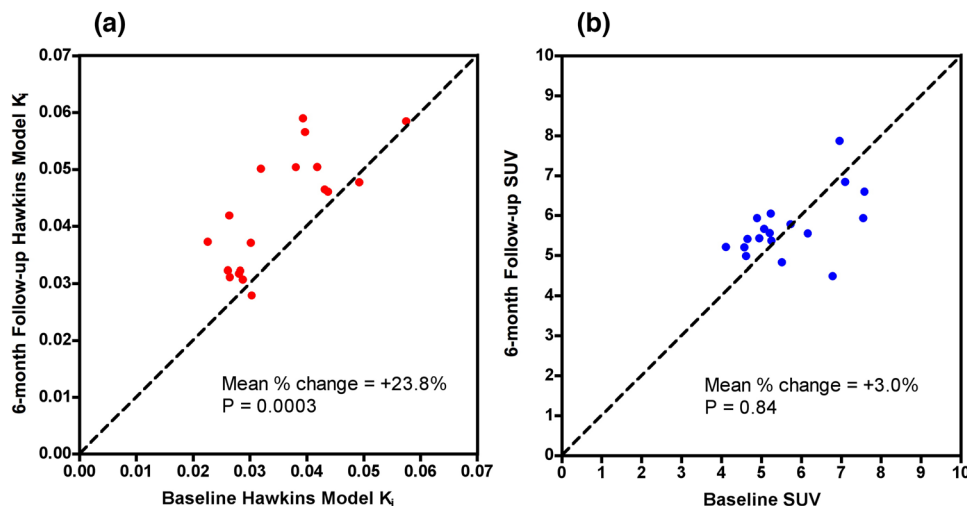
FIGURE 10 (a) The scatter graph of Hawkins model lumbar spine K_i values after six months of treatment with the parathyroid hormone (PTH) analog teriparatide plotted against the baseline measurements. Data is from the study of 18 postmenopausal women whose Patlak and Hawkins model K_i measurements are shown plotted in Figure 8b. The mean percentage increase in K_i is 23.8%. (b) A similar plot of the follow-up and baseline measurements of the lumbar spine mean standardized uptake value (SUV_{mean}). The mean percentage increase in SUV_{mean} is 3.0%.

TABLE 1 Some clinical applications of [^{18}F]NaF PET/CT

Metabolic bone disorders	osteoporosis, Paget's disease
Chronic kidney disease mineral and bone disorder (CKD-MBD)	
Metastatic bone disease	breast cancer, prostate cancer
Autoimmune diseases	ankylosing spondylitis, rheumatoid arthritis
Fracture healing	
Atypical femoral shaft fractures	
Orthopedic applications	
Vascular calcification	
Osteogenic bone disorder	fibrodysplasia ossificans progressiva (FOP)
Medication-related	osteonecrosis of the jaw (MRONJ)

6 | EXAMPLES OF CLINICAL APPLICATIONS

[^{18}F]NaF PET/CT scans have been used to study a wide variety of metabolic, metastatic, and other bony diseases, often with particular attention paid to quantifying response to treatment (Table 1).

Figures 8b and 9b showed data from one such study, which looked at how postmenopausal women with low bone density (i.e., osteopenia) at the spine or hip responded to 6 months of treatment with teriparatide (TPT). TPT, a parathyroid hormone analog used to treat osteoporosis, is a bone anabolic agent that promotes bone formation and results in high tracer uptake throughout the skeleton on the radionuclide bone scan.[60] Further data from the same study is shown in Figure 10a, which shows Hawkins model lumbar spine K_i measurements obtained from follow-up 60-min dynamic scans acquired after 6 months treatment with TPT plotted against the baseline measurements. Figure 10b shows data from the same study plotted as the 60-min lumbar spine SUV measurements.

There is a striking difference between the two sets of findings, with an average response to treatment of 23.8% ($P = 0.0003$) for K_i compared with a 3.0% ($P = 0.84$) change in SUV. The difference between the K_i and SUV findings is explained by a 20% lower concentration of [^{18}F]NaF in plasma following treatment with TPT due to the greater proportion of the injected tracer laid down in cortical bone in the peripheral skeleton. As explained in the Introduction, in circumstances where a treatment or a disease process has a sufficiently potent effect on bone metabolism to alter the AIF, then a measurement of K_i gives a truer indication of the state of the regional bone turnover than a measurement of SUV. In a subsequent study, Frost et al.[61] performed 60-min dynamic scans at the hips and a static scan at the lumbar spine following 12 weeks of TPT treatment in a similar group of postmenopausal women. Different skeletal sites responded differently, with increases of 50.7% ($P = 0.001$) in cortical bone in the femoral shaft and 17.8% ($P < 0.001$) in the lumbar spine. Studies of response to treatment using biochemical markers of bone turnover show that measurements of markers of bone formation reach their maximum response after around 12 weeks of treatment. It is advisable not to perform [^{18}F]NaF PET scans to study response to treatment earlier than this.

Another application that has attracted interest is the potential of [^{18}F]NaF PET/CT scans for the investigation of patients with CKD-MBD, in particular, whether

measurements of lumbar spine K_i can differentiate patients with high turnover disease from those with adynamic bone disease (ABD).[65,89] Existing diagnostic methods based on measurements of PTH and bone-specific alkaline phosphatase have low sensitivity and specificity. The challenge has been to find a biomarker that correlates with bone turnover and is superior to PTH for evaluating bone metabolism in patients with CKD. An interesting aspect of such studies is that, as well as providing data on potential diagnostic thresholds for K_i for the detection of ABD, they involve direct measurements of bone turnover using bone biopsy with tetracycline labeling at the iliac crest. Despite the fact that these studies are small, with no more than 20-30 participants in each, and that the scatter plots of K_i against histomorphometric measurements of bone formation are inevitably quite noisy, there is a consistent trend of a positive relationship, which confirms the basic tenet that quantitative [^{18}F]NaF PET provides a measure of bone formation rate.

We have not included a table of typical K_i values since numerical values are sensitive to the method used (e.g., the systematic difference between the Patlak and Hawkins model values shown in Figure 8b). Values probably vary with age, gender, disease status and treatment, and being too specific might be misleading. Interestingly, we find little systematic difference between women with and without osteoporosis. It is possible that a higher rate of bone turnover in women with osteoporosis is countered by the smaller mass of bone tissue.

7 | CONCLUSION

In conclusion, we have described the procedures involved in measuring bone metabolism with [^{18}F]NaF PET by using a short static scan combined with a semi-population method of deriving the AIF and have provided a spreadsheet to facilitate the calculations. We hope that this simplified method will make the technique more accessible to researchers and clinicians and promote wider use of [^{18}F]NaF PET in the clinic as well as in research settings.

REFERENCES
1. Heaney RP. Is the paradigm shifting? *Bone*. 2003;33(4):457-465. doi:10.1016/s8756-3282(03)00236-9
2. Azad GK, Siddique M, Taylor B, et al. Is response assessment of breast cancer bone metastases better with measurement of 18F-Fluoride metabolic flux than with measurement of 18F-Fluoride PET/CT SUV? *J Nucl Med*. 2019;60(3):322-327. doi:10.2967/jnumed.118.208710
3. Puri T, Blake GM. Letter regarding "Correlation of the quantitative methods for the measurement of bone uptake and plasma clearance of 18 F-NaF using positron emission tomography. Systematic review and meta-analysis. *Eur J Radiol*. 2022;147:110138. doi:10.1016/j.ejrad.2021.110138
4. Doot RK, Muzi M, Peterson LM, et al. Kinetic analysis of 18F-fluoride PET images of breast cancer bone metastases. *J Nucl Med*. 2010;51(4):521-527. doi:10.2967/jnumed.109.070052
5. Yu EY, Duan F, Muzi M, et al. Castration-resistant prostate cancer bone metastasis response measured by 18F-fluoride PET after treatment with dasatinib and correlation with progression-free survival: results from American College of Radiology Imaging Network 6687. *J Nucl Med*. 2015;56(3):354-360. doi:10.2967/jnumed.114.146936
6. Muzi M, O'Sullivan F, Perk TG, et al. Whole-Body [18F]-Fluoride PET SUV imaging to monitor response to dasatinib Therapy in castration-resistant prostate cancer bone metastases: secondary results from ACRIN 6687. *Tomography*. 2021;7(2):139-153. doi:10.3390/tomography7020013
7. Salgarello M, Lunardi G, Inno A, et al. 18F-NaF PET/CT imaging of brain metastases. *Clin Nucl Med*. 2016;41(7):564-565. doi:10.1097/RLU.0000000000001186
8. Arlot M, Meunier PJ, Boivin G, et al. Differential effects of teriparatide and alendronate on bone remodeling in postmenopausal women assessed by histomorphometric parameters. *J Bone Miner Res*. 2005;20(7):1244-1253. doi:10.1359/JBMR.050309
9. Compston JE, Croucher PI. Histomorphometric assessment of trabecular bone remodelling in osteoporosis. *Bone Miner*. 1991;14(2):91-102. doi:10.1016/0169-6009(91)90086-f
10. Dempster DW, Cosman F, Kurland ES, et al. Effects of daily treatment with parathyroid hormone on bone microarchitecture and turnover in patients with osteoporosis: a paired biopsy study. *J Bone Miner Res*. 2001;16(10):1846-1853. doi:10.1359/jbmr.2001.16.10.1846
11. Lindsay R, Zhou H, Cosman F, Nieves J, Dempster DW, Hodsman AB. Effects of a one-month treatment with PTH(1-34) on bone formation on cancellous, endocortical, and periosteal surfaces of the human ilium. *J Bone Miner Res*. 2007;22(4):495-502. https://doi.org/10.1359/jbmr.070104
12. Jiang Y, Zhao JJ, Mitlak BH, Wang O, Genant HK, Eriksen EF. Recombinant human parathyroid hormone (1-34) [teriparatide] improves both cortical and cancellous bone structure. *J Bone Miner Res*. 2003;18(11):1932-1941. https://doi.org/10.1359/jbmr.2003.18.11.1932
13. Puri T, Frost ML, Curran KM, et al. Differences in regional bone metabolism at the spine and hip: a quantitative study using (18)F-fluoride positron emission tomography. *Osteoporos Int*. 2013;24(2):633-639. https://doi.org/10.1007/s00198-012-2006-x

14. Frost ML, Blake GM, Cook GJ, Marsden PK, Fogelman I. Differences in regional bone perfusion and turnover between lumbar spine and distal humerus: (18)F-fluoride PET study of treatment-naïve and treated postmenopausal women. *Bone*. 2009;45(5):942-948. doi:10.1016/j.bone.2009.07.081

15. Garnero P, Hausherr E, Chapuy MC, et al. Markers of bone resorption predict hip fracture in elderly women: the EPIDOS Prospective Study. *J Bone Miner Res*. 1996;11(10):1531-1538. https://doi.org/10.1002/jbmr.5650111021

16. Beck-Jensen JE, Kollerup G, Sørensen HA, Pors Nielsen S, Sørensen OH. A single measurement of biochemical markers of bone turnover has limited utility in the individual person. *Scand J Clin Lab Invest*. 1997;57(4):351-359. https://doi.org/10.3109/00365519709099408

17. Frost ML, Fogelman I, Blake GM, Marsden PK, Cook GJR. Dissociation between global markers of bone formation and direct measurement of spinal bone formation in osteoporosis. *J Bone Miner Res*. 2004;19(11):1797-1804. https://doi.org/10.1359/JBMR.040818

18. Lenora J, Norrgren K, Thorsson O, Wollmer P, Obrant KJ, Ivaska KK. Bone turnover markers are correlated with total skeletal uptake of 99mTc-methylene diphosphonate (99mTc-MDP). *BMC Med Phys*. 2009;9:3. https://doi.org/10.1186/1756-6649-9-3

19. Puri T, Frost ML, Cook GJ, Blake GM. [18F] Sodium Fluoride PET Kinetic Parameters in Bone Imaging. *Tomography*. 2021;7(4):843-854. https://doi.org/10.3390/tomography7040071

20. Narita N, Kato K, Nakagaki H, Ohno N, Kameyama Y, Weatherell JA. Distribution of fluoride concentration in the rat's bone. *Calcif Tissue Int*. 1990;46(3):200-204. https://doi.org/10.1007/BF02555045

21. Grant FD, Fahey FH, Packard AB, Davis RT, Alavi A, Treves ST. Skeletal PET with 18F-fluoride: applying new technology to an old tracer. *J Nucl Med*. 2008;49(1):68-78. https://doi.org/10.2967/jnumed.106.037200

22. Boivin G, Farlay D, Khebbab MT, Jaurand X, Delmas PD, Meunier PJ. In osteoporotic women treated with strontium ranelate, strontium is located in bone formed during treatment with a maintained degree of mineralization. *Osteoporos Int*. 2010;21(4):667-677. https://doi.org/10.1007/s00198-009-1005-z

23. Messa C, Goodman WG, Hoh CK, et al. Bone metabolic activity measured with positron emission tomography and [18F]fluoride ion in renal osteodystrophy: correlation with bone histomorphometry. *J Clin Endocrinol Metab*. 1993;77(4):949-955. https://doi.org/10.1210/jcem.77.4.8408470

24. Aaltonen L, Koivuviita N, Seppänen M, et al. Correlation between 18F-Sodium Fluoride positron emission tomography and bone histomorphometry in dialysis patients. *Bone*. 2020;134:115267. https://doi.org/10.1016/j.bone.2020.115267

25. Siddique M, Blake GM, Frost ML, et al. Estimation of regional bone metabolism from whole-body 18F-fluoride PET static images. *Eur J Nucl Med Mol Imaging*. 2012;39(2):337-343. https://doi.org/10.1007/s00259-011-1966-y

26. Puri T, Siddique MM, Frost ML, Moore AEB, Blake GM. A short dynamic scan method of measuring bone metabolic flux using [18F]NaF PET. *Tomography*. 2021;7(4):623-635. https://doi.org/10.3390/tomography7040053

27. Grados F, Brazier M, Kamel S, Mathieu M, Hurtebize N, Maamer M, Garabédian M, Sebert JL, Fardellone P. Prediction of bone mass density variation by bone remodeling markers in postmenopausal women with vitamin D insufficiency treated with calcium and vitamin D supplementation. *J Clin Endocrinol Metab*. 2003;88(11):5175-9. https://doi.org/10.1210/jc.2002-021968

28. O'Connor JP, Aboagye EO, Adams JE, et al. Imaging biomarker roadmap for cancer studies. *Nat Rev Clin Oncol*. 2017;14(3):169-186. https://doi.org/10.1038/nrclinonc.2016.162

29. Keyes JW Jr. SUV: standard uptake or silly useless value? *J Nucl Med*. 1995;36(10):1836-1839.

30. Hawkins RA, Choi Y, Huang SC, et al. Evaluation of the skeletal kinetics of fluorine-18-fluoride ion with PET. *J Nucl Med*. 1992;33(5):633-642.

31. Siddique M, Frost ML, Blake GM, et al. The precision and sensitivity of (18)F-fluoride PET for measuring regional bone metabolism: a comparison of quantification methods. *J Nucl Med*. 2011;52(11):1748-1755. https://doi.org/10.2967/jnumed.111.093195

32. Patlak CS, Blasberg RG. Graphical evaluation of blood-to-brain transfer constants from multiple-time uptake data. Generalizations. *J Cereb Blood Flow Metab*. 1985;5(4):584-590. https://doi.org/10.1038/jcbfm.1985.87

33. Brenner W, Vernon C, Muzi M, et al. Comparison of different quantitative approaches to 18F-fluoride PET scans. *J Nucl Med*. 2004;45(9):1493-500.

34. Puri T, Blake GM, Frost ML, et al. Comparison of six quantitative methods for the measurement of bone turnover at the hip and lumbar spine using 18F-fluoride PET-CT. *Nucl Med Commun*. 2012;33(6):597-606. https://doi.org/10.1097/MNM.0b013e3283512adb

35. Raijmakers P, Temmerman OP, Saridin CP, et al. Quantification of 18F-Fluoride kinetics: evaluation of simplified methods. *J Nucl Med*. 2014;55(7):1122-1127. https://doi.org/10.2967/jnumed.113.135269

36. Blake GM, Puri T, Siddique M, Frost ML, Moore AEB, Fogelman I. Site specific measurements of bone formation using [18F] sodium fluoride PET/CT. *Quant Imaging Med Surg*. 2018;8(1):47-59. doi:10.21037/qims.2018.01.02

37. Blake GM, Frost ML, Fogelman I. Quantitative radionuclide studies of bone. *J Nucl Med*. 2009;50(11):1747-1750. https://doi.org/10.2967/jnumed.109.063263

38. Blake GM, Siddique M, Frost ML, Moore AE, Fogelman I. Radionuclide studies of bone metabolism: do bone uptake and bone plasma clearance provide equivalent measurements of bone turnover? *Bone*. 2011;49(3):537-542. https://doi.org/10.1016/j.bone.2011.05.031

39. Administration of Radioactive Substances Advisory Committee. Notes for guidance on the clinical administration of radiopharmaceuticals and use of sealed radioactive sources. Accessed June 1 2022 https://www.gov.uk/arsac

40. Basic anatomical and physiological data for use in radiological protection: reference values. A report of age- and gender-related differences in the anatomical and physiological characteristics of reference individuals. ICRP Publication 89. *Ann ICRP*. 2002;32(3-4):5-265.

41. Menendez MI, Moore RR, Abdel-Rasoul M, et al. [18F] Sodium Fluoride Dose Reduction Enabled by Digital Photon Counting PET/CT for Evaluation of Osteoblastic Activity. *Front Med (Lausanne)*. 2022 Jan 12;8:725118. https://doi.org/10.3389/fmed.2021.725118

42. Badawi RD, Shi H, Hu P, et al. First Human Imaging Studies with the EXPLORER Total-Body PET Scanner. *J Nucl Med*. 2019 Mar;60(3):299-303. https://doi.org/10.2967/jnumed.119.226498

43. Zhang X, Xie Z, Berg E, et al. Total-Body Dynamic Reconstruction and Parametric Imaging on the uEXPLORER. *J Nucl Med*. 2020 Feb;61(2):285-291. https://doi.org/10.2967/jnumed.119.230565

44. Schneck DJ. An outline of cardiovascular structure and function. *The Biomedical Engineering Handbook, Fourth Edition, Biomedical Engineering Fundamentals, Section 1 Physiologic systems*, 1-1. Editors Bronzino JD & Petrson DR. CRC Press. 2015.

45. Taves DR. Electrophoretic mobility of serum fluoride. *Nature*. 1968 Nov 9;220(5167):582-583. https://doi.org/10.1038/220582a0

46. Bettinardi V, Presotto L, Rapisarda E, Picchio M, Gianolli L, Gilardi MC. Physical performance of the new hybrid PET/CT Discovery-690. *Med Phys*. 2011;38(10):5394-5411. https://doi.org/10.1118/1.3635220

47. Wong JM, Puri T, Siddique MM, et al. Comparison of ordered-subset expectation maximization and filtered back projection reconstruction based on quantitative outcome from dynamic [18F]NaF PET images. *Nucl Med Commun*. 2021 ;42(6):699-706. https://doi.org/10.1097/MNM.0000000000001393

48. Bruckbauer T, Christian B, Mantil J, Valk P. 9:-9:15. 3D Data Acquisition for Whole Body Images on the ECAT HR+. *Clin Positron Imaging*. 2000;3(4):145. https://doi.org/10.1016/s1095-0397(00)00057-1

49. Strobel K, Rüdy M, Treyer V, Veit-Haibach P, Burger C, Hany TF. Objective and subjective comparison of standard 2-D and fully 3-D reconstructed data on a PET/CT system. *Nucl Med Commun*. 2007;28(7):555-559. https://doi.org/10.1097/MNM.0b013e328194f1e3

50. Bettinardi V, Mancosu P, Danna M, et al. Two-dimensional vs three-dimensional imaging in whole body oncologic PET/CT: a Discovery-STE phantom and patient study. *Q J Nucl Med Mol Imaging*. 2007;51(3):214-223.

51. Strother SC, Casey ME, Hoffman EJ. Measuring PET scanner sensitivity: relating count rates to image signal-to-noise ratios using noise equivalents counts. *IEEE Transactions on Nuclear Science*. 1990;37(2):783-788. https://doi.org/10.1109/23.106715

52. Zaidi H. *Quantitative Analysis in Nuclear Medicine Imaging*. New York: Springer; 2006.

53. Frost ML, Cook GJ, Blake GM, Marsden PK, Benatar NA, Fogelman I. A prospective study of risedronate on regional bone metabolism and blood flow at the lumbar spine measured by 18F-fluoride positron emission tomography. *J Bone Miner Res*. 2003;18(12):2215-2222. https://doi.org/10.1359/jbmr.2003.18.12.2215

54. Cook GJ, Lodge MA, Marsden PK, Dynes A, Fogelman I. Non-invasive assessment of skeletal kinetics using fluorine-18 fluoride positron emission tomography: evaluation of image and population-derived arterial input functions. *Eur J Nucl Med*. 1999;26(11):1424-1429. https://doi.org/10.1007/s002590050474

55. Phelps ME, Huang SC, Hoffman EJ, Selin C, Sokoloff L, Kuhl DE. Tomographic measurement of local cerebral glucose metabolic rate in humans with (F-18)2-fluoro-2-deoxy-D-glucose: validation of method. *Ann Neurol*. 1979;6(5):371-388. https://doi.org/10.1002/ana.410060502

56. Puri T, Greenhalgh TA, Wilson JM, et al. [18F]Fluoromisonidazole PET in rectal cancer. *EJNMMI Res*. 2017 Sep 20;7(1):78. https://doi.org/10.1186/s13550-017-0324-x

57. Puri T, Blake GM, Siddique M, et al. Validation of new image-derived arterial input functions at the aorta using 18F-fluoride positron emission tomography. *Nucl Med Commun*. 2011 Jun;32(6):486-495. https://doi.org/10.1097/MNM.0b013e3283452918

58. Puri T, Blake GM, Frost ML, et al. Validation of image-derived arterial input functions at the femoral artery using 18F-fluoride positron emission tomography. *Nucl Med Commun*. 2011;32(9):808-817. https://doi.org/10.1097/MNM.0b013e328349716f

59. Blake GM, Siddique M, Puri T, et al. A semipopulation input function for quantifying static and dynamic 18F-fluoride PET scans. *Nucl Med Commun*. 2012;33(8):881-888. https://doi.org/10.1097/MNM.0b013e3283550275

60. Frost ML, Siddique M, Blake GM, et al. Differential effects of teriparatide on regional bone formation using (18)F-fluoride positron emission tomography. *J Bone Miner Res*. 2011;26(5):1002–1011. https://doi.org/10.1002/jbmr.305

61. Frost ML, Moore AE, Siddique M, et al. ¹⁸F-fluoride PET as a non-invasive imaging biomarker for determining treatment efficacy of bone active agents at the hip: a prospective, randomized, controlled clinical study. *J Bone Miner Res*. 2013;28(6):1337-1347. https://doi.org/10.1002/jbmr.1862

62. Chen K, Bandy D, Reiman E, et al. Noninvasive quantification of the cerebral metabolic rate for glucose using positron emission tomography, 18F-fluoro-2-deoxyglucose, the Patlak method, and an image-derived input function. *J Cereb Blood Flow Metab*. 1998;18(7):716-23. https://doi.org/10.1097/00004647-199807000-00002

63. Vrist MH, Bech JN, Lauridsen TG, Fynbo CA, Theil J. Comparison of [18F] NaF PET/CT dynamic analysis methods and a static analysis method including derivation of a semi-population input function for site-specific measurements of bone formation in a population with chronic kidney disease-mineral and bone disorder. *EJNMMI Res*. 2021;11(1):117. https://doi.org/10.1186/s13550-021-00859-7

64. Peters MJ, Wierts R, Jutten EM, Halders SG, Willems PC, Brans B. Evaluation of a short dynamic 18F-fluoride PET/CT scanning method to assess bone metabolic activity in spinal orthopedics. *Ann Nucl Med*. 2015;29(9):799-809. https://doi.org/10.1007/s12149-015-1008-0

65. Aaltonen L, Koivuviita N, Seppänen M, Burton IS, Kröger H, Löyttyniemi E, Metsärinne K. Bone Histomorphometry and 18F-Sodium Fluoride Positron Emission Tomography Imaging: Comparison Between only Bone Turnover-based and Unified TMV-based Classification of Renal Osteodystrophy. *Calcif Tissue Int*. 2021;109(6):605-614. https://doi.org/10.1007/s00223-021-00874-9

66. Thomas MD, Bailey DL, Livieratos L. A dual modality approach to quantitative quality control in emission tomography. *Phys Med Biol*. 2005;50(15):N187-194. https://doi.org/10.1088/0031-9155/50/15/N03

67. Cook GJ, Lodge MA, Blake GM, Marsden PK, Fogelman I. Differences in skeletal kinetics between vertebral and humeral bone measured by 18F-fluoride positron emission tomography in postmenopausal women. *J Bone Miner Res*. 2000;15(4):763-769. https://doi.org/10.1359/jbmr.2000.15.4.763

68. Haddock B, Fan AP, Jørgensen NR, Suetta C, Gold GE, Kogan F. Kinetic [18F]-Fluoride of the Knee in Normal Volunteers. *Clin Nucl Med*. 2019;44(5):377-385. https://doi.org/10.1097/RLU.0000000000002533

69. Piert M, Machulla HJ, Jahn M, Stahlschmidt A, Becker GA, Zittel TT. Coupling of porcine bone blood flow and metabolism in high-turnover bone disease measured by [(15)O]H(2)O and [(18)F]fluoride ion positron emission tomography. *Eur J Nucl Med Mol Imaging*. 2002;29(7):907-914. https://doi.org/10.1007/s00259-002-0797-2

70. Piert M, Zittel TT, Machulla HJ, et al. Blood flow measurements with [(15)O]H2O and [18F]fluoride ion PET in porcine vertebrae. *J Bone Miner Res*. 1998;13(8):1328-1336. https://doi.org/10.1359/jbmr.1998.13.8.1328

71. Siddique M, Frost ML, Moore AE, Fogelman I, Blake GM. Correcting (18)F-fluoride PET static scan measurements of skeletal plasma clearance for tracer efflux from bone. *Nucl Med Commun*. 2014;35(3):303-310. https://doi.org/10.1097/MNM.0000000000000047

72. Funck T, Larcher K, Toussaint PJ, Evans AC, Thiel A. APPIAN: Automated pipeline for PET image analysis. *Front Neuroinform*. 2018;12:64. https://doi.org/10.3389/fninf.2018.00064

73. López-González FJ, Paredes-Pacheco J, Thurnhofer-Hemsi K, et al. QModeling: a Multiplatform, Easy-to-Use and Open-Source Toolbox for PET Kinetic Analysis. *Neuroinformatics*. 2019;17(1):103-114. https://doi.org/10.1007/s12021-018-9384-y

74. Tjerkaski J, Cervenka S, Farde L, Matheson GJ. Kinfitr-an open-source tool for reproducible PET modelling: validation and evaluation of test-retest reliability. *EJNMMI Res*. 2020;10(1):77. https://doi.org/10.1186/s13550-020-00664-8

75. AMIDE: Medical Imaging Data Examiner. Accessed June 1, 2022 http://amide.sourceforge.net/

76. Carimas. Accessed June 1, 2022 https://turkupetcentre.fi/carimas/

77. COMKAT (Compartmental Model Kinetic Analysis Tool). Accessed June 1, 2022. https://nmmitools.org/2019/01/01/comkat/

78. KMtool: Kinetic Modeling Toolbox. Accessed June 1, 2022. https://mscipio.github.io/project/kmtool/

79. UCLA Tracer Kinetic Model Fitting (TKMF) Program. . Accessed June 1, 2022. https://nmmitools.org/2019/01/01/ucla_tkmf/

80. Cheng C, Alt V, Pan L, et al. Application of F-18-sodium fluoride (NaF) dynamic PET-CT (dPET-CT) for defect healing: a comparison of biomaterials in an experimental osteoporotic rat model. *Med Sci Monit*. 2014;20:1942-1949. doi: 10.12659/MSM.891073

81. Adesanya O, Sprowson A, Masters J, Hutchinson C. Review of the role of dynamic 18F-NaF PET in diagnosing and distinguishing between septic and aseptic loosening in hip prosthesis. *J Orthop Surg Res*. 2015;10:5. https://doi.org/10.1186/s13018-014-0147-7

82. Doris MK, Newby DE. Identification of early vascular calcification with (18)F-sodium fluoride: potential clinical application. *Expert Rev Cardiovasc Ther*. 2016;14(6):691-701 https://doi.org/10.1586/14779072.2016.1151354

83. Jenkins NW, Talbott JF, Shah V, et al. [18F]-Sodium Fluoride PET MR-Based Localization and Quantification of Bone Turnover as a Biomarker for Facet Joint-Induced Disability. *AJNR Am J Neuroradiol*. 2017;38(10):2028-2031. https://doi.org/10.3174/ajnr.A5348

84. Haddock B, Fan AP, Uhlrich SD, et al. Assessment of acute bone loading in humans using [18F]NaF PET/MRI. *Eur J Nucl Med Mol Imaging*. 2019;46(12):2452-2463. https://doi.org/10.1007/s00259-019-04424-2

85. Dyke JP, Garfinkel JH, Volpert L, et al. Imaging of Bone Perfusion and Metabolism in Subjects Undergoing Total Ankle Arthroplasty Using 18F-Fluoride Positron Emission Tomography. *Foot Ankle Int*. 2019;40(12):1351-1357. https://doi.org/10.1177/1071100719882717

86. Watkins L, MacKay J, Haddock B, et al. Assessment of quantitative [18F]Sodium fluoride PET measures of knee subchondral bone perfusion and mineralization in osteoarthritic and healthy subjects. *Osteoarthritis Cartilage*. 2021;29(6):849-858. https://doi.org/10.1016/j.joca.2021.02.563

87. MacKay JW, Watkins L, Gold G, Kogan F. [18F]NaF PET-MRI provides direct in-vivo evidence of the association between bone metabolic activity and adjacent synovitis in knee osteoarthritis: a cross-sectional study. *Osteoarthritis Cartilage*. 2021;29(8):1155-1162. https://doi.org/10.1016/j.joca.2021.04.014

88. Jassel IS, Siddique M, Frost ML, Moore AEB, Puri T, Blake GM. The influence of CT and dual-energy X-ray absorptiometry (DXA) bone density on quantitative [18F] sodium fluoride PET. *Quant Imaging Med Surg*. 2019;9(2):201-209. doi:10.21037/qims.2019.01.01

89. Frost ML, Compston JE, Goldsmith D, et al. (18)F-fluoride positron emission tomography measurements of regional bone formation in hemodialysis patients with suspected adynamic bone disease. *Calcif Tissue Int*. 2013;93(5):436-447. https://doi.org/10.1007/s00223-013-9778-7

SUPPORTING INFORMATION

Additional supporting information can be found online in the Supporting Information section at the end of this article.